IEEE Photonics Journal
An IEEE Photonics Society Publication

Open Access

Freeform Surface Graded Optimization of Deformable Mirrors in Integrated Zoom and Image Stabilization System Through Vectorial Ray Tracing and Image Point Freezing Method

Volume 12, Number 1, February 2020

Yan Ning
Yao Hu
Xuemin Cheng
Qun Hao
Yang Cheng
Tengfei Li
Xin Tao

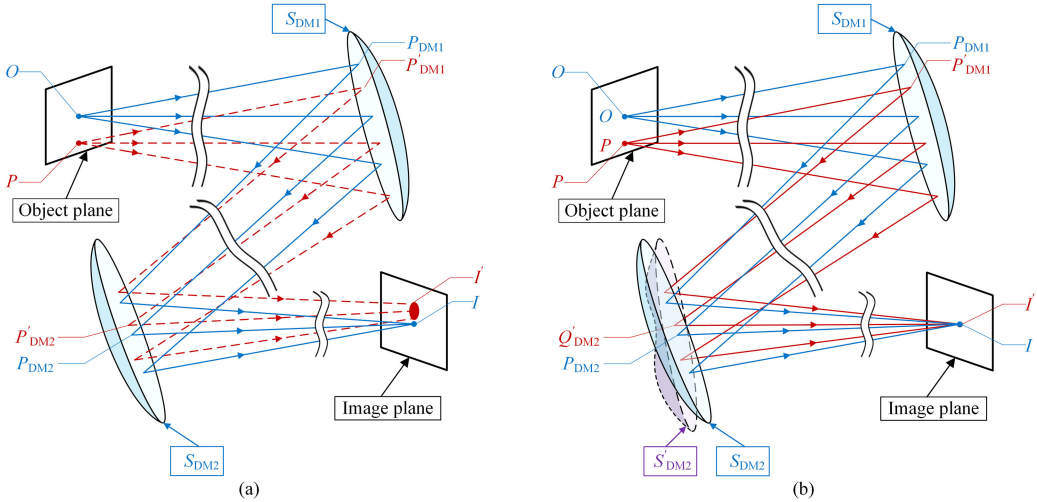

DOI: 10.1109/JPHOT.2019.2960300

Freeform Surface Graded Optimization of Deformable Mirrors in Integrated Zoom and Image Stabilization System Through Vectorial Ray Tracing and Image Point Freezing Method

Yan Ning,[1] **Yao Hu**,[1] **Xuemin Cheng**,[2] **Qun Hao**,[1] **Yang Cheng**,[1] **Tengfei Li**,[3] **and Xin Tao**[1]

[1]Beijing Key Laboratory for Precision Optoelectronic Measurement Instrument and Technology, School of Optics and Photonics, Beijing Institute of Technology, Beijing 100081, China
[2]Graduate School at Shenzhen, Tsinghua University, Shenzhen 518055, China
[3]China North Vehicle Research Institute, Beijing 100072, China

DOI:10.1109/JPHOT.2019.2960300

Manuscript received November 4, 2019; accepted December 12, 2019. Date of publication December 17, 2019; date of current version January 9, 2020. This work was supported in part by the Natural National Science Foundation of China under Grants 51735002 and 61735003, and in part by the Shenzhen Science and Technology Innovation Program under Grant JCYJ20170412171011187.
Corresponding author: Qun Hao (e-mail: qhao@bit.edu.cn).

Abstract: Integrated zoom and image stabilization system based on deformable mirrors (DMs) has advantages of miniaturization, rapid response and low energy consumption. Integrating the two capabilities on one DM-based imaging system poses considerable challenges. First, limited DM stroke will result in limited changeable aberration correction value for zoom and image stabilization. Second, the DM-based off-axis imaging system suffers a simple relative movement between optical axis and objects caused by carrier vibration may result in complicated optical system aberrations. To address these challenges, a reasonable assignment of the changeable aberration correction value for zoom and image stabilization is needed. Image stabilization and aberration correction in DM-based off-axis imaging system, should be considered when translation or rotation occurs. To troubleshoot the assignment issues of the correcting aberrations, we propose a graded optimization method which comprises two steps. To troubleshoot the image stabilization and aberration correction issues, we introduce vectorial ray tracing method and image point freezing principle to transform the aberration correction problem into an optimization problem of image coordinates. With the proposed method, we construct practical integrated freeform surfaces of DMs for a space camera with three mirrors. The sagittal heights of designed DM surface profiles are limited within their available stroke.

Index Terms: Deformable mirror, integrated zoom and image stabilization system, advanced optics design, graded optimization.

1. Introduction

Zoom and image stabilization are two important capacities for many imaging systems, such as reconnaissance camera integrated into high-speed moving vehicles and space camera that works on vibrating aircraft. Moreover, miniaturization, compact size, low energy consumption and high

speed have become the main trends in the development of such cameras [1]. Thus, the study of an integrated zoom and image stabilization system, which has advantages of miniaturization, rapid response and low energy consumption, is necessary. Optical elements with variable surface profiles enable the exploration of such imaging system because of its advantages of miniaturization, power consumption, stability, speed and costs [2]. As a useful and important nonmoving optical element with variable surface profiles and precise modulation accuracy [3], deformable mirror (DM) can be applied in integrated zoom and image stabilization systems.

Use of DMs in zoom and image stabilization systems has been proven feasible, respectively.

A substantial body of research has been recently published on optical zoom systems using two DMs. Seidl *et al.* [4] designed an all-reflective, unobscured optical-power zoom objective with 3× magnification, which solely used reflective elements and was free from chromatic aberrations. Lu *et al.* [5] designed a power-variable zoom system with 2.5× zoom ratio, which could achieve zoom adjustment in fractions of a millisecond. Su *et al.* [6]–[9] applied DM-based zoom system to commercial mobile devices with 2× zoom ratio and adopted two ionic polymer metal composite DMs to successfully achieve 1.6× magnification. However, the DM-based zoom system has relatively small range of zoom magnification because of its limited optical power range. However, reports have shown the feasibility of using two DMs in optical zoom systems and have proven the advantage of DM-based zoom system in achieving zoom adjustment at unprecedented speeds.

In addition to zoom capability, image stabilization capability is indispensable for imaging system when relative movement between the optical axis and objects is observed [10]–[12]. For example, an imaging system that works in high-speed moving vehicles or vibrating aircraft will suffer from undesired mutual translation or rotation, which causes image blurring within exposure time. The application of optical stabilization components driven by the mechanical device to provide tilt compensation is a popular solution in maintaining the stability of the optical axis. Great progress has been achieved in the research of optical stabilization components, such as tilt mirror, fast steering mirror and liquid lens [13]–[15]. DMs can generate additional aberrations to provide tilt compensation because its surface can be arbitrarily changed after manufacturing and can generate complex surface profiles compared with these components.

In our previous work, we analyzed the paraxial properties and investigated the quick zooming characteristics of zoom systems using the optical power of the optical element as the independent variable in the zoom equation to design a novel zoom system with two DMs [16]. Moreover, we presented an optical stabilization system based on DMs that can stabilize images [17]. We constructed the mathematical model using relative parameters to calculate the compensation angle of the DM for image stabilization. However, the integration issues have not yet been performed in our previous study. Thus, we focus on integrating zoom and image stabilization capabilities in one imaging system in this work.

Integrating zoom and image stabilization capabilities on one DM-based imaging system pose considerable challenges. Firstly, limited DM stroke will result in limited changeable aberration correction value for zoom and image stabilization. Secondly, DM-based imaging system often uses off-axis structure. Thus, a simple mutual translation or rotation between the imaging system and the objects caused by carrier vibration may result in complicated optical system aberrations. Such aberrations can be hardly compensated when solely using tilt aberrations. Therefore, the integration of zoom and image stabilization capacities in one DM-based imaging system cannot be achieved by directly superposing the correcting aberrations for zoom and tilt aberrations for image stabilization. To address these challenges, a reasonable assignment of the changeable aberration correction value for zoom and image stabilization is needed. Image stabilization, as well as aberration correction in DM-based off-axis imaging system, should be considered when translation or rotation occurs.

To troubleshoot the assignment issues of the correcting aberrations, we propose a graded optimization method which comprises two steps, namely, first-order design of DM freeform surface profiles for zoom and second-order design of DM freeform surface profile for integrated zoom and image stabilization. To troubleshoot image stabilization and aberration correction issues, we

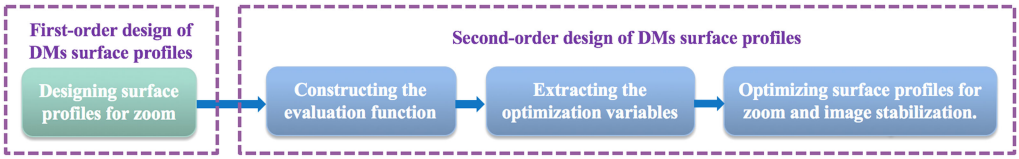

Fig. 1. Outline of graded optimization framework for integrated freeform surfaces of DMs.

introduce vectorial ray tracing method and image point freezing principle to transform the aberration correction problem into an optimization problem of image coordinates.

The remainder of this paper is organized as follows. Section 2 describes the graded optimization method for integrated freeform surface of DMs in an unobscured off-axis imaging system with two DMs. Section 3 discusses an optimization example of integrated DM surface profiles in an all-reflective unobscured space camera using the proposed method. Section 4 analyzes and discusses the optimization results. Section 5 provides the conclusions of this study.

2. Graded Optimization Method

2.1 Optimization Setup

The construction of integrated freeform surfaces of DMs consists of the first-order and second-order design of DMs surface profiles (Fig. 1).

The first-order design is performed to calculate the DM surface profiles for zoom capability. Standard Zernike polynomials are utilized to represent the DM surface profiles. We deduce the relationship between the system-expected optical power and the Zernike coefficients of DM surface profiles for zoom capability based on matrix optic theory.

The second-order design is performed to optimize the DM surface profile for integrated zoom and image stabilization. The aberration correction problem is transformed into an optimization problem of image coordinates, and the optimization issues undergo troubleshooting through the nonlinear optimization algorithm. More specifically, we establish an optimization model and construct practical integrated freeform surface of DMs to maintain the zoom capability and adapt to the mutual translation or rotation, thereby keeping the image point constant when translation or rotation occurs in the integrated system. The optimization model consists of three procedures, namely, constructing the evaluation function, extracting the optimization variables, and optimizing the integrated DM surface profile. First, we establish the evaluation function with the coordinates of the image points before and after the system translation or rotation occurs to the imaging system. The feature incident rays are defined and the feature emergent rays (coordinates and direction vectors) are calculated using vectorial ray tracing method to acquire the coordinates of the image points. Second, we extract the correcting aberrations that affect image stabilization and require less DM stroke amount as the optimization variables. This procedure is performed by iterative processes of the constructed evaluation function on the basis of geometrical optics and nonlinear optimization method. Lastly, the integrated DM surface profile was obtained by assigning the extracted correcting aberrations on DM surface profile for zoom capability.

The graded optimization of DM freeform surface for integrated zoom and image stabilization system is described thoroughly in the following sections.

2.2 First-Order Design of DM Surface Profiles

The initial structural design of an unobscured off-axis imaging system is indispensable previous to graded optimization of DMs surface profiles. We perform the design of an unobscured imaging system on the basis of a certain classical off-axis system design method [18]–[22] according to practical application requirements. For unobscured off-axis imaging system, some general design usually considers two steps [4]. First, optical elements are assumed to have zero thickness and only

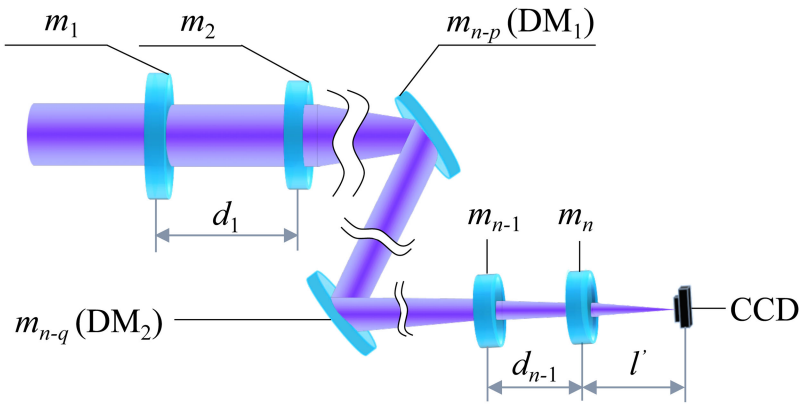

Fig. 2. Schematic of an unobscured off-axis imaging system with two DMs (DM$_1$ and DM$_2$). Double wavy lines in the imaging system indicate fixed optical elements on either side of the DMs. d_j is the distance between adjacent components, where $j = 1, 2, \ldots, n-1$.

paraxial rays are considered. In this way element optical powers and spacings are determined. Second, in conjunction with the aberration theory, the appropriate decenter and tilt angle of elements are determine to ensure that there is no obscuration occurs.

After determining the initial structure of the unobscured off-axis imaging system, we calculate practical zoom surface profile of two DMs in the designed imaging system. We deduce the relationship between the system-expected optical power and the Zernike coefficients of DM surface profiles for zoom capability on the basis of matrix optics theory [23]. The unobscured, off-axis imaging system with two DMs (DM$_1$ and DM$_2$) and optical elements with fixed focal length is depicted in Fig. 2. m_i denotes the optical elements in the imaging system and φ_i denotes their optical power, where $i = 1, \ldots, n-p, \ldots, n\text{-}q, \ldots, n$ ($p > q$). It is assumed that the elements m_{n-p} and m_{n-q} in the optical system are DM$_1$ and DM$_2$ respectively. φ_{DM1} and φ_{DM2} denote the optical power of DM$_1$ and DM$_2$ (i.e., $\varphi_{DM1} = \varphi_{n-p}$ and $\varphi_{DM2} = \varphi_{n-q}$). d_j is distance between adjacent components, where $j = 1,2, \ldots, n\text{-}1$. l' is the back focal length of the imaging system. To ensure the zoom capability, the focal length of the imaging system with nonmoving elements should vary by changing the optical powers of DM$_1$ and DM$_2$ meanwhile the back focal length remains stable.

Each optical element in the imaging system can be expressed by a 2×2 matrix

$$M_i = \begin{pmatrix} 1 & 0 \\ -\varphi_i & 1 \end{pmatrix}. \tag{1}$$

Furthermore, the separations can be written as

$$T_j = \begin{pmatrix} 1 & d_j \\ 0 & 1 \end{pmatrix}. \tag{2}$$

The paraxial matrix M of the complete system is the product of the matrices in reversed order

$$M = \begin{pmatrix} A & B \\ C & D \end{pmatrix} = M_n \cdot T_{n-1} \cdot \ldots \cdot M_{n-p} \cdot T_{n-p-1} \cdot \ldots \cdot M_{n-q} \cdot T_{n-q-1} \cdot \ldots M_2 \cdot T_1 \cdot M_1. \tag{3}$$

With the relation [4]

$$\begin{cases} \varphi_S = -C \\ l' = -\frac{A}{C} \end{cases}, \tag{4}$$

when the expected optical power of the imaging system φ_{S} is determined, the optical power variation governing equation of the two DMs (φ_{DM1} and φ_{DM2}) can be deduced

$$\begin{cases} \varphi_{DM1} = f(\varphi_S, l', \varphi_i, d_j) \\ \varphi_{DM2} = g(\varphi_S, l', \varphi_i, d_j) \end{cases} \quad (i \neq n-p, i \neq n-q). \tag{5}$$

The micro actuators of the DM are controlled to move up or down along the vertical direction of the mirror by applying bias voltage, thereby transforming the DM shape into a rotationally symmetrical aspheric surface with different radii. This process is performed to change the optical power of the DMs for possessing zoom capability. We use the standard Zernike polynomials to represent the DM surface profile [24] for the following reasons. First, the aberrations expressed by Zernike polynomials correspond well to Seidel aberrations. Second, the probable asymmetric aberrations in common off-axis imaging system can be well represented by Zernike polynomials. Thus, the DM surface profile is represented by standard Zernike polynomials as

$$Z = \sum_{j=1}^{n} C_j \times Z_j, \tag{6}$$

where Z denotes the sagittal height of the DM surface profile, Z_j represents the jth order Zernike term, and C_j is the coefficient of Z_j.

On the basis of aspheric definition [25], we extract the 5th, 13th, and 25th terms of the standard Zernike polynomials; these terms exhibit significant contributions to DM optical power from the correctable standard Zernike terms of DMs. Given that most commercially available DMs can correct low-order aberrations with relatively higher dynamic range and correction quality in comparison with correcting high-order aberrations, we solely choose the lowest-order one among the aberrations that exhibit significant contributions to DM optical power. Finally, the 5th term of the standard Zernike polynomials is extracted as the correcting aberration for zoom. The coefficient of the 5th term (i.e., defocus–field curvature aberration) is expressed as C_5. The relationship between the coefficient C_{5i} and the optical power of the two DMs is deduced on the basis of the conicoid polynomial fitting model, shown as follows:

$$C_{5i} = \frac{\varphi_{DMi}}{8} \quad (i = 1, 2). \tag{7}$$

By Eq. (5) and Eq. (7), the relationship between the system-expected optical power and the Zernike coefficients of DM surface profiles for zoom capability can be deduced. Moreover, the designed DM surface profiles for zoom capability are referred to as S_{DM1} and S_{DM2}.

2.3 Second-Order Design of DM Surface Profile

This section establishes an optimization model and designs practical DM surface profile for integrated zoom and image stabilization system. The entire design process consists of three steps, namely, constructing the evaluation function, extracting the optimization variables, and optimizing the integrated DM surface profile.

2.3.1 Construction of Evaluation Function: We acquire the coordinates of the image points using vectorial ray tracing method to construct the evaluation function. The ray tracing paths in the imaging system are shown in Fig. 3. $O(x, y, z)$ is an on-axis object point, that is, an object point on the 0° field of view (FOV), where (x, y, z) is the coordinate of an arbitrary point on the object plane. It is assumed that m feature incident rays starting from $O(x, y, z)$ and propagating through the surfaces in the imaging system (i.e., DM_1, DM_2 and other fixed optical elements) are traced, where m is the number of feature incident rays. P_{DM1} and P_{DM2} are the intersection points of the feature incident and DMs in the imaging system, respectively. m feature emergent rays converge to the image point set $I(x_m, y_m, z_m)$ through the reflection on the surfaces in the imaging system, where

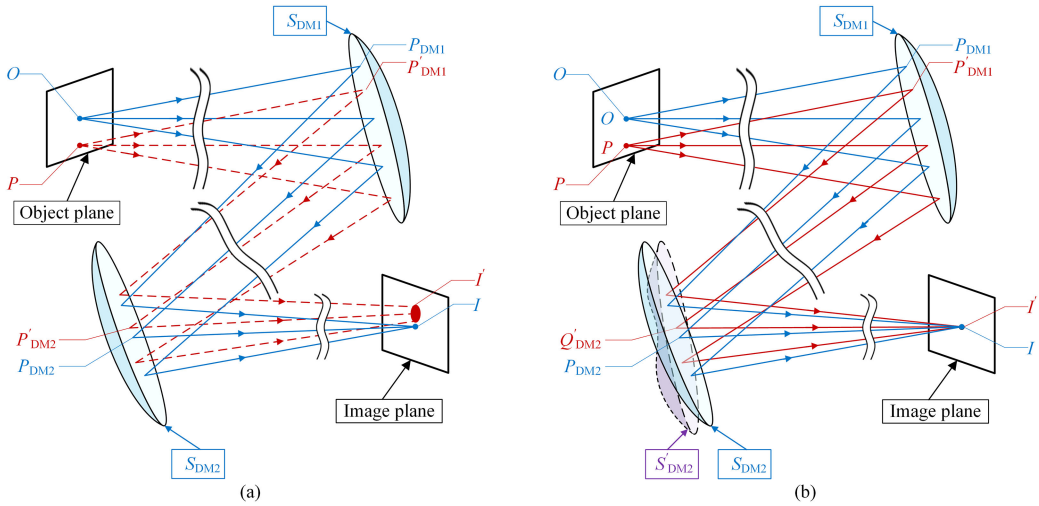

Fig. 3. Ray tracing paths in the off-axis imaging system. (a) Ray tracing paths with and without translation or rotation in the imaging system. Double wavy lines in the imaging system indicate fixed optical elements on either side of the DMs. Blue rotationally symmetrical aspheric surfaces show the designed surface profiles S_{DM1} and S_{DM2} for zoom. Blue solid lines are ray tracing paths without the occurrence of translation or rotation; these ray tracing paths trace rays from point O, which is the initial object point, through the imaging system toward image point I. Points P_{DM1} and P_{DM2} are the intersections of the incident and reflected rays on the DMs, respectively. Red dashed lines are ray tracing paths with the occurrence of translation or rotation; these ray tracing paths trace rays from point P, which is the shifted point location on the object plane, thereby tracing the optical path toward blurry spot I' using the unchanged profiles of DM surfaces. Points P'_{DM1} and P'_{DM2} are the intersections of the incident and reflected rays on the DMs, respectively. (b) Ray tracing paths for image stabilization using DMs. Blue rotationally symmetrical aspheric surfaces and blue solid lines still illustrate the designed surface profiles S_{DM1} and S_{DM2} for zoom and ray tracing paths without the occurrence of translation or rotation. Purple aspheric surface shows the changed profile S'_{DM2} of the DM surface for image stabilization. Red solid lines are ray tracing paths for image stabilization; these ray tracing paths trace rays from point O and maintain the image point of $I'(x'_m, y'_m, z'_m)$ as $I(x_m, y_m, z_m)$ using the changed profile S'_{DM2} of the DM surface. Point Q'_{DM2} is one of the intersections of the incident and reflected rays on the S'_{DM2}.

(x_m, y_m, z_m) is the coordinate of an arbitrary point in the image point set I. With the well-designed DM surface profiles for zoom, the image point set $I(x_m, y_m, z_m)$ is a convergent spot (i.e., the image point set $I(x_m, y_m, z_m)$ comprises m image points with extraordinary close coordinates). When translation or rotation occurs to the imaging system, the on-axis object point $O(x, y, z)$ shifts to an off-axis object point $P(x', y', z')$, as shown in Fig. 3(a). On the basis of geometric optics, P_{DM1} and P_{DM2} shift to P'_{DM1} and P'_{DM2}, respectively, and the image point of $P(x', y', z')$ is no longer a convergent spot $I(x_m, y_m, z_m)$ but a blurry spot $I'(x'_m, y'_m, z'_m)$ consists of m discrete image points, as shown in Fig. 3(a). Therefore, modifying DM surfaces to adapt the translation or rotation (i.e., achieve image stabilization) is necessary.

One DM with a larger available stroke is selected to achieve image stabilization and maintain the surface profile for zoom capability. We applied DM for image stabilization because its variable surface profile and precise modulation accuracy [3]. DMs with larger available stroke also hold more potential in providing greater amplitude of correcting aberrations [26]. In this manner, the limited changeable aberration correction value is reasonably assigned, and the design procedure is simplified. Suppose that DM_2 has a larger available stroke after generating surface profile for zoom capability. Then, it is selected to achieve image stabilization. As shown in Fig. 3(b), the modified surface profile of DM_2 is referred to as the DM surface profile for image stabilization (S'_{DM2}), which can maintain the image point of $P(x', y', z')$ as $I(x_m, y_m, z_m)$. Point Q'_{DM2} is the corresponding intersection point of the feature incident rays and the modified surface profile S'_{DM2} of DM_2 in the imaging system.

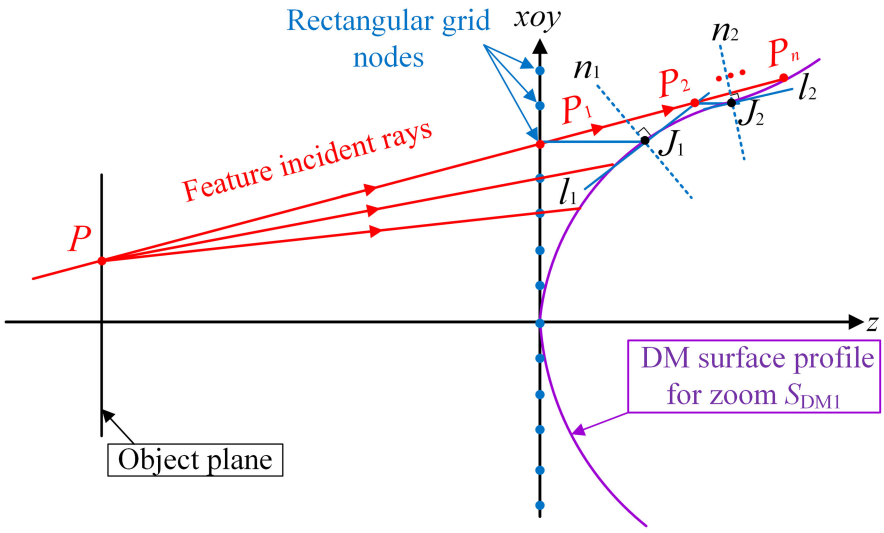

Fig. 4. Schematic of tracing the feature incident rays on DM_1 surface profile. Purple aspheric surface shows the designed surface profile S_{DM1} for zoom. P is the shifted object point. P_1 and P_n are the intersection points of feature incident rays and *xoy* plane, respectively. J_1 and J_2 are the intersection points of parallel line to the *z*-axis and the DM_1 surface profile, respectively. l_1 and l_2 are the tangent lines of the DM_1 surface profile. n_1 and n_2 are the normal of the DM_1 surface profile.

The surface is modified with the correcting aberrations that affect image stabilization on the DM_2 surface profile for zoom capability (S_{DM2}), which can be expressed as follows

$$S'_{DM2} = S_{DM2} + \sum_{j=1}^{n} M_j \times Z_j, \tag{8}$$

where $M_j \times Z_j$ represents the correcting aberrations that affect image stabilization.

An evaluation function is constructed to assess and verify the image stabilization capability of the modified surface profile S'_{DM2}. Although several optical design software programs (e.g., Zemax and CODE V) are commercially available for performing vectorial ray tracing, obtaining the coordinates of all the feature incident rays on the DM simultaneously is difficult. Therefore, we use MATLAB software (MathWorks, Inc.) to perform vectorial ray tracing. Different from ray tracing on simple surfaces, vectorial ray tracing is difficult to perform using an algebraic method on the DM because its surface profile is a complex aspheric surface. Thus, vectorial ray tracing should be performed in a general numerically iterative manner [27]. For instance, the schematic of tracing the feature incident rays on DM_1 surface is shown in Fig. 4. The feature incident ray is defined by connecting the object points from FOVs and rectangular grid nodes on a plane. The plane is the projective plane of DM_1 surface profile in the *xoy* direction. After defining the feature incident rays, vectorial ray tracing of the incident feature light rays is performed.

Initially, the intersection point of feature incident ray and *xoy* plane is denoted as P_1. A line starting from P_1 and parallel to the *z*-axis is drawn. The intersection point of this line and the DM_1 surface profile is denoted as J_1. Next, the tangent line crossing point J_1 of the DM_1 surface profile is expressed as l_1. The intersection point of feature incident ray and tangent line l_1 is expressed as P_2. Finally, whether P_2 is on the DM_1 surface profile can be determined by calculating the distance between P_2 and P_1. If the distance is less than a threshold ε (i.e., $|P_2 - P_1| < \varepsilon$), then the geometric iterative algorithm ends, and the intersection point P_2 is regarded as on the DM_1 surface profile. Otherwise, the geometric iterative algorithm continues until the intersection point P_n satisfies $|P_n - P_{n-1}| < \varepsilon$. On the basis of the above geometric iterative algorithm, the intersection point coordinates P_n on the DM_1 surface profile of feature incident rays are obtained. Then, a vector formula [28] is applied and combined with the general numerically iterative algorithm to trace the feature incident

rays on the DM surface. The ray coordinates $I'(x_m', y_m', z_m')$ on the image plane can be achieved by tracing the feature incident rays that pass through the surface profiles in the imaging system in sequence.

The image $I(x_m, y_m, z_m)$ of the on-axis object point $O(x, y, z)$ can also be calculated using the vectorial ray tracing method. Different correcting aberrations are assigned for modifying the S_{DM2} surface profile to possess the image stabilization ability, that is, to fix the image point of P on I instead of I'. An evaluation function is established to determine whether the modified surface S'_{DM2} meets the requirement of image stabilization; the evaluation function can be expressed as follows

$$F_0 = \sum \left| I'(x_m', y_m', z_m') - I(x_m, y_m, z_m) \right|, \tag{9}$$

where F_0 is the evaluation function for zero-degree FOV. $I(x_m, y_m, z_m)$ is the ideal image point set consists of m image points with extraordinary close coordinates. $I'(x_m', y_m', z_m')$ is the shifted image point set consists of m discrete image points. Only when the value of F_0 closes to zero that the changed surface S'_{DM2} meets the requirement of image stabilization, that is, image stabilization is achieved.

The previous analysis for image stabilization is based on conjugate points on zero-degree FOV. However, from a practical perspective, numerous conjugate points exist from different FOVs in an imaging system. Therefore, the evaluation function F of all FOVs should be calculated, as shown as follows

$$F = \sum_{r=0}^{u} F_r, \tag{10}$$

where r is the index of the FOVs in the system, and u is the number of FOVs. Only when the value of F closes to zero that the modified surface S'_{DM2} can achieve the image stabilization for all FOVs.

2.3.2. Extraction of Optimization Variables: After constructing the evaluation function, we extract the correcting aberrations (expressed with standard Zernike polynomials) that affect image stabilization and require less DM stroke amount as the optimization variables. We perform this process because different correcting aberrations exhibit particular effects on image stabilization.

The process of extracting correcting aberrations includes two parts. First, we confirm the extraction scope of standard Zernike polynomials according to the correction performance of commercially available DMs. Then, we divide the confirmed standard Zernike polynomials into different categories in a certain mode. For instance, the confirmed standard Zernike polynomials can be divided into rotational and nonrotational symmetric items, low-items and high-order items, and longitudinal and transverse items.

On the basis of Eq. (8), each correcting aberration is expressed as $M_j \times Z_j$. The extraction is achieved by performing iterative processes of the constructed evaluation function. Specifically, the correcting aberrations in different categories are initially assigned to DM_2, and the aberration coefficients can be calculated until F is iteratively optimized to approach 0. The evaluation functions before and after iteration are denoted as F and F', respectively. On the basis of Eq. (6), the reduction of evaluation function (i.e., $\Delta F = F' - F$) is calculated. ΔZ is the increment of the sagittal height of S'_{DM2} and is calculated based on Eq. (8). The expected correcting category can be extracted by comparing ΔF and ΔZ that correspond to the assigned aberration categories. As an effective optimization method [29], [30], simulated annealing algorithm is selected to perform the iterative processes.

Then, we compare ΔF and ΔZ of different correcting aberration categories and extract the category that contribute considerably to the evaluation function reduction and contribute slightly to the sagittal height increment of S'_{DM2} as most appropriate category for image stabilization.

The second part of the extraction of correcting aberrations is the exclusion of inappropriate aberrations from the selected aberration category. After comparing ΔF and ΔZ of each correcting aberration in the selected aberration category, we extract the correcting aberrations that contribute considerably to the evaluation function reduction and contribute slightly to the sagittal height

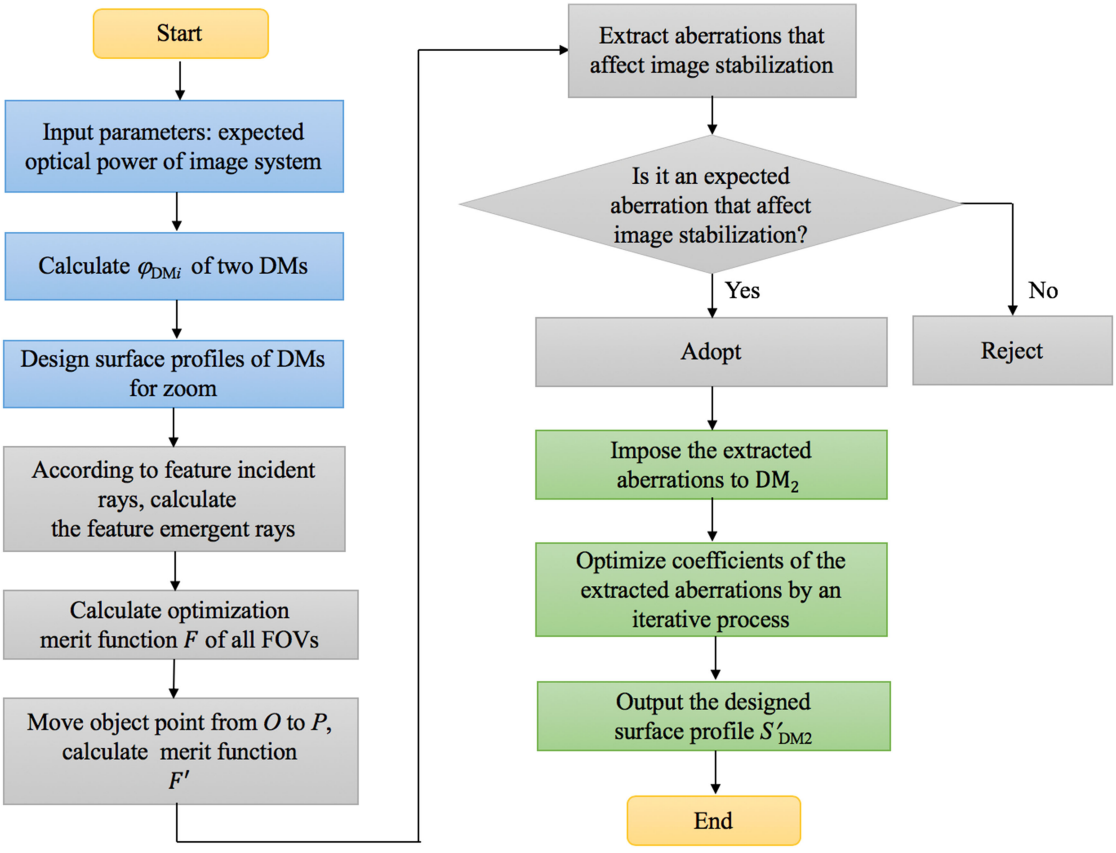

Fig. 5. Flowchart of graded optimization for DMs in integrated zoom and image stabilization system. The blue boxes represent the calculation process of the DM surface profile for zoom capability; the gray boxes represent the process of extracting the correcting aberrations that affect image stabilization and require less DM stroke amount; and the green boxes show the optimization processes of DM surface profile for image stabilization while maintaining the DM surface profile for zoom capability.

increment of S'_{DM2} as optimization variables. Then, the other aberrations are regarded as the inappropriate aberrations and are excluded from the selected aberration category.

2.3.3 Optimization of Integrated DM Surface Profile: The last process entails the extraction of correcting aberrations and subsequently using them to modify DM_2 from S_{DM2} to S'_{DM2} for image stabilization. The extracted aberrations in Section 2.3.2 are assigned to DM_2 for image stabilization and for maintaining the DM_2 surface profile for zoom capability. The coefficients of the extracted correcting aberrations are further optimized with simulated annealing algorithm to minimize the value of the evaluation function F. From the preceding analysis, we establish an optimization model and design practical DM surface profiles for integrated zoom and image stabilization system.

The freeform surface graded optimization of DMs in integrated zoom and image stabilization system is completed. The flowchart that clearly represents the design process is depicted in Fig. 5.

3. Design Example

In this section, the freeform surface graded optimization of DMs in an all-reflective, unobscured space camera for integrated zoom and image stabilization is performed to demonstrate the validity of the proposed method.

Previous to graded optimization of DMs surface profiles, we perform the design step of an all-reflective, unobscured space camera with a FOV of 2° and an expected initial focal length of 60 mm.

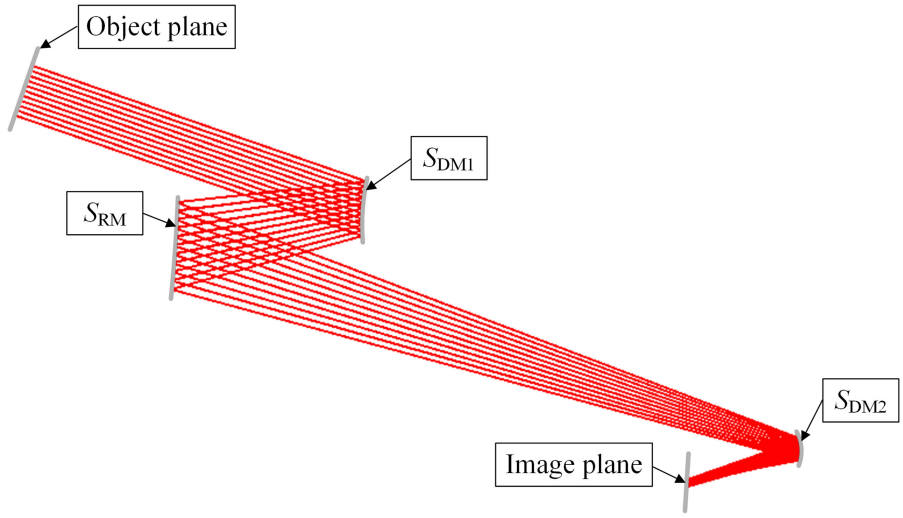

Fig. 6. Design of the all-reflective, unobscured space camera. S_{DM1}: surface profile of deformable mirror 1; S_{RM}: reflective mirror with a fixed focal length; S_{DM2}: surface profile of deformable mirror 2. The initial focal length is 60 mm, and the FOV is approximately 2°.

TABLE 1
Structural Parameters of the All-Reflective, Unobscured Space Camera

	Distance /mm	Optical power/mm^{-1}	Alpha tilt/(°)
Mirror 1 (DM_1)	32.3727		-15
Mirror 2 (RM)	109.3465	0.0171	16
Mirror 3 (DM_2)	17.2138		-15
Image plane			15

For the purpose of simplifying the optical structure, we designed an all-reflective, unobscured space camera consists three mirrors based on the design theory of an unobscured reflective imaging system [18]. The designed space camera with two DMs (DM_1 and DM_2) and one reflective mirror (RM) with a fixed focal length is depicted in Fig. 6. The structural parameters of the camera are shown in Table 1.

The expected goal of zoom capability is that the focal length of the camera ranges from 40 mm to 80 mm. Limited by its stroke range, DMs are appropriate for refined image stabilization wherein the imaging system and the objects are translated or rotated within a mill radian precision [17]. The expected goal of image stabilization capability in this paper is that the camera is free of 1 mrad optical axis trembling, which is the typical value of refined image stabilization.

3.1 Design of Two DM Surface Profiles for Zoom Capability

The surface profiles of two DMs for zoom capability are initially designed. On the basis of Eq. (5) and Eq. (7), relationship between the system-expected optical power and the Zernike coefficients

TABLE 2
Parameters of Imaging System for Zoom Capability

Expected focal length	Calculated C_5 for DM_1	Calculated C_5 for DM_2	Achieved focal length
40.00 mm	−0.0040 mm	-2.2829×10^{-4} mm	39.95 mm
80.00 mm	−0.0043 mm	-6.8001×10^{-4} mm	80.01mm

Fig. 7. Experimental results of system zooming capability. (a) Image at 40 mm focal length. (b) Image at 80 mm focal length.

C_5 of DM surface profiles for zoom capability is deduced

$$\begin{cases} C_{51} = \frac{\varphi_{DM1}}{8} = \frac{\varphi_S l' - d_2\varphi_{RM} - 1}{8d_1 + 8d_2 - 8d_1 d_2 \varphi_{RM}} \\ C_{52} = \frac{\varphi_{DM2}}{8} = \frac{d_1\varphi_{DM1}\varphi_{RM} + \varphi_S - \varphi_{DM1} - \varphi_{RM}}{8d_1\varphi_{DM1} + 8d_2(\varphi_{DM1} + \varphi_{RM} - d_1\varphi_{DM1}\varphi_{RM}) - 8} \end{cases}. \tag{11}$$

On the basis of Eq. (11), we obtained coefficients C_5 of the defocus–field curvature aberration. Then we designed surface profiles for zoom on the basis of Eq. (6). With the designed surface profiles of DMs, the corresponding focal length of space camera is calculated through the optical design software CODE V. The space camera parameters for zoom capability are shown in Table 2.

Simulation experiments are performed using the 2D image simulation function in CODE V to achieve the two expected focal length of the space camera. The simulation results are shown in Fig. 7. In Fig. 7(a), the image size after assigning the calculated C_{5i} ($i = 1,2$) corresponding to focal length of 40 mm to the two DMs is 2.2926 mm $\times$ 2.2926 mm. In Fig. 7(b), the image size after assigning the calculated C'_{5i} corresponding to focal length of 80 mm to the two DMs is 4.5818 mm $\times$ 4.5818 mm. Therefore, the zoom ratio of this space camera is 2.00$\times$ (4.5818 mm/2.2926 mm). The result is found consistent with the expected goal, which indicates the validity of the proposed method in designing two DM surface profiles for zoom capability.

3.2 Optimization of One DM Surface Profile for Image Stabilization

In this section, the space camera with 80 mm focal length is taken as an example to analyze the optimization of DM surface profile for image stabilization. On the basis of the principle mentioned in section 2.3.1, DM_2 is selected to achieve image stabilization and maintain the surface profile for zoom capability because it has a larger available stroke than DM_1 has. Notably, the available stroke of DMs is related to their inherent stroke, and stroke has been used for zoom capability.

3.2.1 Construction of Evaluation Function: Tracing the incident rays is initially performed to achieve image stabilization. The projective plane of DM_1 surface profile in the *xoy*-direction is meshed with 50 $\times$ 50 rectangular grid nodes, and the feature incident rays are drawn by connecting the object point and the nodes. The feature emergent rays can be determined by successively

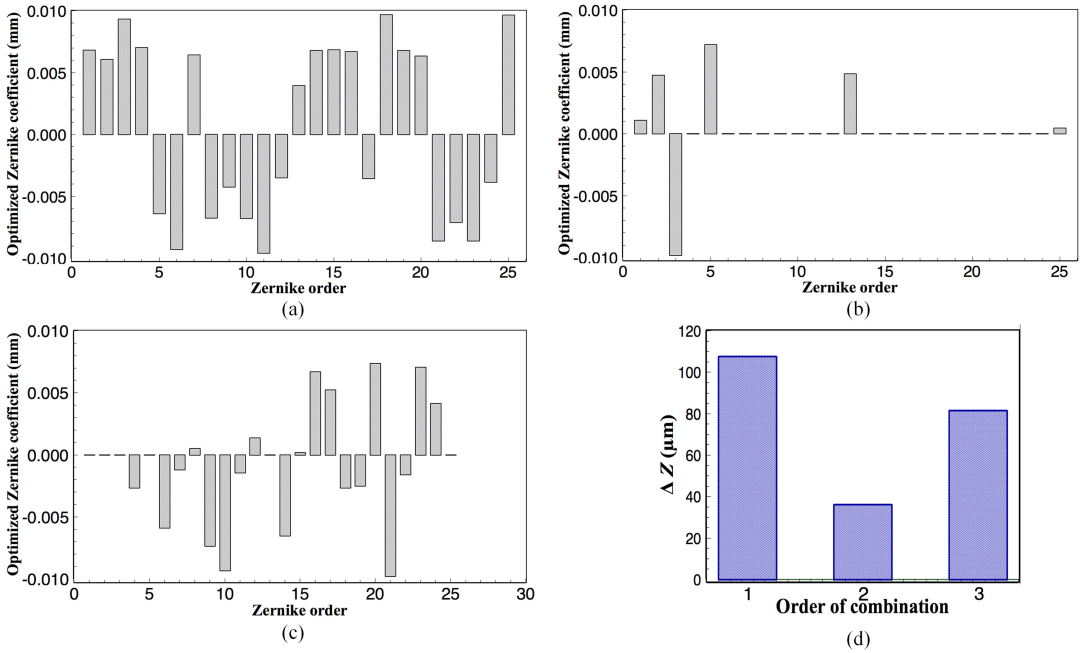

Fig. 8. Extracted results of the first 25 items of Zernike standard polynomials in the first part. Optimized Zernike coefficient of (a) first 25 items of standard Zernike polynomials; (b) rotational symmetric items in the first 25 items of standard Zernike polynomials; (c) nonrotational symmetric items in the first 25 items of standard Zernike polynomials; (d) sagittal height increment of the DM_2 surface profile; order of combinations 1–3 denote the combination of the first 25 items of standard Zernike polynomials, rotational symmetric items in the first 25 items of standard Zernike polynomials, and nonrotational symmetric items in the first 25 items of standard Zernike polynomials, respectively. Note: Here, ΔF of the three combinations in (a)–(c) are not depicted in Fig. 8, which are all deduced from 150.3569 mm to 0 mm.

tracing the feature incident rays that pass through the surface profiles in the space camera. We use MATLAB software to perform vectorial ray tracing of the feature incident rays. The tracing result is shown in Fig. 6. The ray coordinates $l_m\,(x_m,\ y_m,\ z_m)$ on the image plane are calculated by spatial ray vector formulas.

An optical axis of 1 mrad, trembling along the *y*-axis, is introduced to the imaging system (i.e., the optical axis rotates along the *y*-axis). The valuation function *F* before image stabilization is 150.3569 mm, which is calculated according to Eq. (10). The corresponding sagittal height of surface S_{DM2} is 35.3458 μm, which is calculated according to Eq. (8).

3.2.2. Extraction of Optimization Variables: The correcting aberrations that affect image stabilization and require less DM stroke amount are extracted on the basis of the analysis the first 25 items of standard Zernike polynomials. These items are selected because they can meet the requirements of image stabilization in most cases. Moreover, the latter items of standard Zernike polynomials are difficult to generate by most commercial DMs.

The process of extracting correcting aberrations includes two parts. First, the first 25 items of standard Zernike polynomials are divided into two categories, namely, the rotational symmetric items (i.e., 1st, 2nd, 3rd, 5th, 13th, and 25th terms of the standard Zernike polynomial) and the nonrotational symmetric items (i.e., the rest of aberrations in the first 25 items of the standard Zernike polynomial). The aberrations in different categories are assigned to DM_2 respectively. All the 25 items are also assigned to DM_2 for comparison. The coefficients of the assigned aberrations in different combinations (i.e., combination of all the first 25 items, the rotational symmetric items, and the nonrotational symmetric items) can be calculated by iterating the evaluation function *F* close to 0 using the simulated annealing algorithm. The calculated coefficients of the assigned aberrations are shown in Fig. 8(a)–7(c). When we assign aberrations in such three combinations

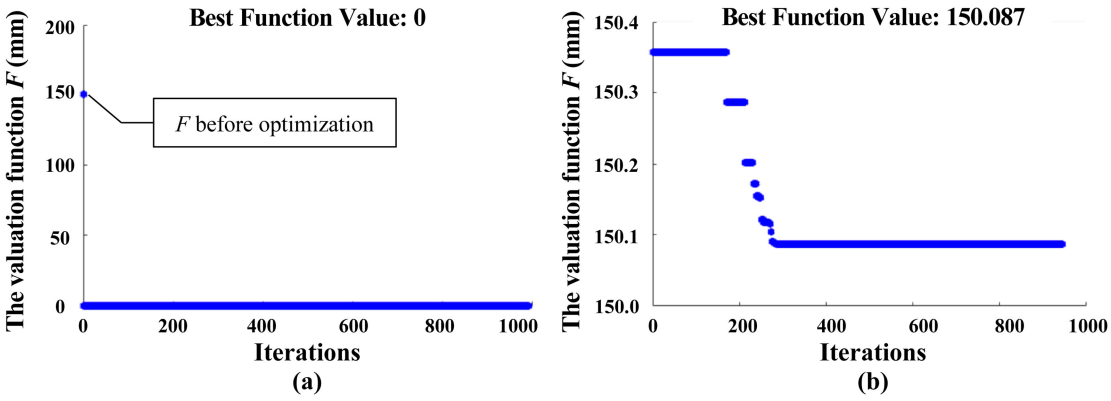

Fig. 9. Optimization results of valuation function *F*. (a) Iterative optimization process of evaluation function *F* using the extracted correcting aberrations (i.e., distortion–tilt aberrations in the *x*- and *y*-axes, defocus–field curvature aberration, and primary spherical aberration). The value of *F* reduces from 150.3569 mm to 0 mm solely with 8 iterations. (b) Iterative optimization process of evaluation function F solely using tilt aberrations (i.e., distortion–tilt aberrations in the *x*- and *y*-axes). The value of *F* reduces from 150.3569 mm to 150.0870 mm after 1000 generations of iterative optimization.

TABLE 3
Coefficients of Surface Profile S'_{DM2} for Zoom and Image Stabilization

Standard Zernike order	M_2	M_3	M_5	M_{13}
Coefficient (mm)	4.076×10^{-3}	-4.444×10^{-3}	-3.088×10^{-3}	4.934×10^{-3}

for image stabilization, the corresponding ΔF of these three conditions all equal to 150.3569 mm. In other words, these combinations can meet the requirements of image stabilization ($F' = 0$). The increment of sagittal height with the three combinations of assigned aberrations is 107.5597 μm, 35.9650 μm, and 81.4452 mm, respectively. The result is shown in Fig. 8(d), which indicates that the rotational symmetric items of the standard Zernike polynomial have a significant contribution to image stabilization and requires the least DM stroke amount among the aforementioned three combinations. Therefore, the rotational symmetric items of the standard Zernike polynomial are primary extracted from the first 25 items.

The second part of the process of extracting correcting aberrations is the exclusion of aberrations that have little contribution to the reduction of evaluation function from the rotational symmetric items. As shown in Fig. 8(b), the coefficient of the 1st item expected to assign to DM_2 is considerably less than others. This result indicates that the 1st item is not required for image stabilization. Moreover, the 25th item is an aberration which is the highest order among the first 25 items and should be avoided. Therefore, these aberrations are excluded from the rotational symmetric items of the standard Zernike polynomials. In this manner, the 2nd, 3rd, 5th, and 13th terms of the standard Zernike polynomial are extracted to achieve image stabilization (i.e., distortion–tilt aberrations in the *x*- and *y*-axes, defocus–field curvature aberration, and primary spherical aberration).

3.2.3. Optimization of Integrated DM Surface Profile: In this section, the aforementioned four extracted aberrations are assigned to DM_2 for image stabilization and for maintaining the DM_2 surface profile for zoom capability. Further coefficient optimization of these aberrations is performed using a simulated annealing algorithm to minimize the value of the evaluation function. As shown in Fig. 9(a), the number of iterations is set to 1000, but the value of *F* reduces from 150.3569 mm to 0 mm solely with 8 iterations. The optimal coefficients of these aberrations are shown in Table 3.

The extracted aberrations assigned to DM_2 reduce the valuation function F from 150.3569 mm to 0 mm. Moreover, the increment in the sagittal height of surface S'_{DM2} is 16.3782 μm. These results indicate that the changed surface profile of DM_2 can meet the requirements of image stabilization and perform a reasonable assignment of the limited changeable aberration correction value of DM_2.

For cross-verification, we compensated aberrations in DM-based off-axis imaging system solely with tilt aberrations (i.e., M_2 and M_3). The optimal coefficients of M_2 and M_3 are 6.127×10^{-3} mm and -2.097×10^{-4} mm respectively. As shown in Fig. 9(b), after 1000 generations of iterative optimization, the value of F reduces from 150.3569 mm to 150.0870 mm. Compared to the optimization result with the extracted aberrations, this result indicates that aberrations in the DM-based off-axis imaging system cannot be compensated when solely using tilt aberrations.

The simulation process of introducing the 1 mrad optical axis that trembles along other directions is not provided in detail due to the limited space available; nevertheless, similar conclusions can be found in these experiments. First, in comparison with nonrotational symmetric aberrations, the rotational symmetric aberrations are more suitable for image stabilization in space camera. Second, when optical axis trembling along other directions occurs to the imaging system, the valuation function F can also be reduced close to 0 with the aberrations extracting from rotational symmetric items. The maximal increment in the sagittal height of surface S'_{DM2} is 30.5743 μm. The analysis of the simulation results indicates that the method proposed in this study is proven reasonable and feasible.

4. Discussions

The graded optimization method through vectorial ray tracing and image point freezing principle proposed in this study focuses on designing the freeform surface of DMs in integrated zoom and image stabilization system. In the process of extracting the optimization variables, which is mentioned in Section 2.3.2, three issues could be further analyzed.

First, in the off-axis imaging system depicted in this study, the rotational symmetric aberrations hold more potential in correcting the nonrotational symmetric aberrations produced by the trembling of the optical axis. The correcting aberrations extracted in Section 3.2.2 cannot be guaranteed as the optimal combination of aberrations; however, this combination can meet the requirement of refined image stabilization and exhibits rationality. Specifically, when certain nonrotational symmetric aberrations are assigned to DM, some rotational symmetric aberrations may be generated in the image plane after such nonrotational symmetric aberrations transmit through the off-axis imaging system. For example, if the assigned aberrations are in the same forms and opposite directions as the aberrations that are expected to be corrected in the off-axis imaging system (i.e., the nonrotational symmetric aberrations caused by the trembling optical axis), then the assigned aberrations may become rotationally symmetric after transmitting to the image plane and it cannot correct the nonrotational symmetric aberrations in the off-axis imaging system. On the contrary, when certain rotational symmetric aberrations are assigned to DM, some nonrotational symmetric aberrations will be generated in the image plane, which are suitable for correcting aberrations in image stabilization.

Second, the extraction result of correcting aberrations that is related to the direction of the trembling optical axis occurs to the imaging system due to the asymmetry of the off-axis imaging system. In other words, when the trembling optical axis with the same value but in different directions are introduced to the off-axis imaging system, the corresponding aberrations to be corrected may be entirely distinctive.

Lastly, the extraction result of correcting aberrations is also related to the structure of the off-axis imaging system. For example, when the off-axis angles in the imaging system and the number and specifications of optical elements suffer from certain changes, the aberrations to be corrected are transformed accordingly.

In conclusion, particular analysis for extracting the correcting aberrations should be considered in an imaging system when the proposed extracting approach cannot satisfy the design requirements for integrated DM surface profiles. For example, when a large trembling optical axis occurs to the

imaging system and the extracted rotational symmetric aberrations fail to meet the requirements for image stabilization, the method of permutation and combination can be considered to extract an effective aberration combination, which is a direction for further study.

5. Conclusion

In this study, we propose a freeform surface graded optimization method of DMs through vectorial ray tracing and image point freezing principle for integrated zoom and image stabilization system. The challenges faced in integrating DMs surface profiles for zoom and image stabilization are transformed into assignment issues of the correcting aberrations and aberration correction issues in off-axis imaging system. The proposed freeform surface optimization method allows for the initial design of two DM surface profiles for zoom. Moreover, the surface profile of one DM with the larger available stroke is optimized for image stabilization and for maintaining zoom capability. Experiments are conducted to demonstrate the capacity of zoom and image stabilization in the proposed imaging system. Given the designed surface profiles of two DMs, the integrated zoom and image stabilization system exhibits a zoom ratio of 2.0$\times$ and is free of 1 mrad trembling optical axis. Furthermore, the freeform surface graded optimization method of DMs through vectorial ray tracing and image point freezing principle could prove to be effective in the design of the integrated system.

Acknowledgment

The authors acknowledge Dr. Cheng Yao for the careful review of the manuscript and helpful discussions.

References

[1] J. Sun, Y Fang, and B. R. Hsueh, "Optical design and multi-objective optimization for U-type 2X zoom projection optics," *Opt. Laser Eng.*, vol. 48, no. 4, pp. 411–420, 2010.
[2] M. Antonín and N. Jiří, "Paraxial imaging properties of double conjugate zoom lens system composed of three tunable-focus lenses," *Opt. Laser Eng.*, vol. 53, pp. 86–89, 2014.
[3] H. Zhao, X. Fan, and G. Zou, "All-reflective optical bifocal zooming system without moving elements based on deformable mirror for space camera application," *Appl. Opt.*, vol. 52, no. 6, pp. 1192–1210, 2013.
[4] K. Seidl, J. Knobbe, and G. Heinrich, "Design of an all-reflective unobscured optical-power zoom objective," *Appl. Opt.*, vol. 48, no. 21, pp. 4097–4107, 2009.
[5] Y. Lu, C. R. Stockbridge, and S. M. Hoffman, "Variable zoom system with aberration correction capability," *J. Modern Opt.*, vol. 59, no. 12, pp. 1049–1055, 2012.
[6] Y. Lin and G. Su, "Optical zoom module based on two deformable mirrors for mobile device applications," *Appl. Opt.*, vol. 51, no. 11, pp. 1804–1810, 2012.
[7] S. Jia and G. Su, "Optical zoom lens module using MEMS deformable mirrors for portable device," *Proc SPIE*, vol. 8488, pp. 1–9, 2012.
[8] Y. Huang, H. Wei, and W. Hsu, "Optical zoom camera module using two poly-dimethylsiloxane deformable mirrors," *Appl. Opt.*, vol. 53, no. 29, pp. 248–256, 2014.
[9] W. Chen, J. Lu, and G. Su, "Ionic polymer metal composite for an optical zoom in a compact camera," *Opt. Exp.*, vol. 23, no. 10, pp. 13265–13277, 2015.
[10] K. Janschek, V. Tchernykh, S. Dyblenko, and B. Harnisch, "Compensation of the attitude instability effect on the imaging payload performance with optical correlators," *Acta Astronaut.*, vol. 52, no. 9, pp. 965–974, 2003.
[11] Y. Suematsu, S. Tsuneta, K. Ichimoto, and T. Shimizu, "Image stabilization system for Hinode (solar-B) solar optical telescope," *Sol. Phys.*, vol. 249, no. 2, pp. 221–232, 2008.
[12] K. Janschek, V. Tchernykh, and S. Dyblenko, "Performance analysis of optomechatronic image stabilization for a compact space camera," *Control Eng. Pract.*, vol. 15, no. 3, pp. 333–347, 2007.
[13] J. R. Taylor, M. S. Anderson, and P. H. Bunton, "High-speed tilt mirror for image stabilization," *Appl. Opt.*, vol. 38, no. 1, pp. 219–223, 1999.
[14] Z. Dong, A. Jiang, and Y. Dai, "Space-qualified fast steering mirror for an image stabilization system of space astronomical telescopes," *Appl. Opt.*, vol. 57, no. 31, pp. 9307–9315, 2018.
[15] E. Simon, P. Craen, and H. Gaton, "Liquid lens enabling real-time focus and tilt compensation for optical image stabilization in camera modules," *Proc. SPIE*, vol. 7716, pp. 1–7, 2010.
[16] Q. Hao, X. Cheng, and K. Du, "Four-group stabilized zoom lens design of two focal-length-variable elements," *Opt. Exp.*, vol. 21, no. 6, pp. 7758–7767, 2013.
[17] Q. Hao, F. Fan, and X. Cheng, "Optical stabilization system based on deformable mirrors for retina-like sensors," *Appl. Opt.*, vol. 55, no. 21, pp. 5623–2329, 2016.

[18] T. Zhang, Y. Wang, and J. Chang, "Design of unobscured reflective zoom system with three mirrors," *Chin. Opt. Lett.*, vol. 8, no. 7, pp. 701–705, 2010.
[19] T. Yang, J. Zhu, and W. Hou, "Design method of freeform off-axis reflective imaging systems with a direct construction process," *Opt. Exp.*, vol. 22, no. 8, pp. 9193–9205, 2014.
[20] Q. Meng, W. Wang, and H. Ma, "Easy-aligned off-axis three-mirror system with wide field of view using freeform surface based on integration of primary and tertiary mirror," *Appl. Opt.*, vol. 53, no. 14, pp. 3028–3034, 2014.
[21] J. Zhu, W. Hou, and X. Zhang, "Design of a low F-number freeform off-axis three-mirror system with rectangular field-of-view," *J. Opt.*, vol. 17, no. 1, pp. 15605–15613, 2015.
[22] T. Yang, J. Zhu, and G. Jin, "Design of a freeform, dual fields-of-view, dual focal lengths, off-axis three-mirror imaging system with a point-by-point construction-iteration process," *Chin. Opt. Lett.*, vol. 14, no. 10, 2016, Art. no. 100801.
[23] J. M. Burch, *Introduction to Matrix Methods in Optics*. Hoboken, NJ, USA: Wiley, 1992, ch. 2.
[24] M. A. Betanzos-Torres, J. Castillo-Mixcóatl, and S. Muñoz-Aguirre, "Adaptive optics system simulator," *Opt. Laser Technol.*, vol. 105, pp. 118–128, 2018.
[25] D Malacara, *Optical Shop Testing*. Hoboken, NJ, USA: Wiley, 2007, ch. 18.
[26] S. B. Ramkumar, M. A. Kamran, and G. Yoon, "Correcting highly aberrated eyes using large-stroke adaptive optics," *J. Refractive Surgery*, vol. 23, no. 9, pp. 947–952, 2007.
[27] H. Gross, *Handbook of Optical Systems*. Hoboken, NJ, USA: Wiley, 2005, ch. 5.
[28] R. R. Shannon, *The Art and Science of Optical Design*. Cambridge Univ. Press, 1997, ch. 2.
[29] A. Torabi and F. Kolahan, "Optimizing pulsed Nd:YAG laser beam welding process parameters to attain maximum ultimate tensile strength for thin AISI316L sheet using response surface methodology and simulated annealing algorithm," *Opt. Laser Technol.*, vol. 103, pp. 300–310, 2018.
[30] F. Zahra, M. Nafiseh, and S. Faraneh, "Simulated annealing optimization in wavefront shaping controlled transmission," *Appl. Opt.*, vol. 57, no. 21, pp. 6233–6242, 2018.